applied sciences

MDPI

Article

Analysis of the Influence of Initial Stress on the Bandgap Characteristics of Configuration-Controllable Metamaterials

Fei Yao [1], Jixiao Wang [2], Qiang Fu [1] and Hongyan Zhang [1,*]

[1] School of Science, Chang'an University, Xi'an 710064, China; 2021112053@chd.edu.cn (F.Y.); 2021112047@chd.edu.cn (Q.F.)
[2] China Nuclear Power Engineering Co., Ltd., Beijing 100089, China; wanggjx_cnpe@hotmail.com
* Correspondence: zhanghongyan@chd.edu.cn; Tel.: +86-029-82334391

Abstract: Configuration-controllable metamaterials are a kind of metamaterials whose bandgaps can be effectively adjusted through configuration control, but the configuration changes also produce initial stress. In this paper, the distribution of the initial stress of the configuration-controllable metamaterial under axial displacement and the influence of initial stress on the band gap characteristics of the structure were analyzed using numerical and experimental methods. The results show that initial stress has a significant influence on the bandgap characteristics, and the position and width of the bandgap change with the magnitude of the initial stress. The bandgap distribution of the structure after considering the initial stress is more consistent with the reported experimental results. The influence of initial stress on bandgap cannot be ignored. When the compressive loading displacement is 10 mm, the frequency range of the first bandgap is 262 Hz–310 Hz and that of the second bandgap is 394 Hz–405 Hz. And the frequency range of the first and second bandgaps will be converted into 254 Hz–291 Hz and 391 Hz–400 Hz when considering initial stress. The initial stress generated by compression deformation reduces the frequency of the structural bandgap. The beginning and ending frequencies of the first bandgap will move toward low frequencies, and the first bandgap will close when the compression displacement reaches 30 mm. The initial stress generated by tensile deformation increases the frequency of the structural bandgap. The beginning and ending frequencies of the first bandgap move toward high frequencies, and the bandgap will close when the tensile displacement is 30 mm.

Keywords: metamaterials; initial stress; bandgap characteristics; configuration-controllable metamaterials

check for updates

Citation: Yao, F.; Wang, J.; Fu, Q.; Zhang, H. Analysis of the Influence of Initial Stress on the Bandgap Characteristics of Configuration-Controllable Metamaterials. *Appl. Sci.* **2023**, *13*, 11137. https://doi.org/10.3390/app132011137

Academic Editor: Aliaksandr Shaula

Received: 2 September 2023
Revised: 28 September 2023
Accepted: 4 October 2023
Published: 10 October 2023

Copyright: © 2023 by the authors. Licensee MDPI, Basel, Switzerland. This article is an open access article distributed under the terms and conditions of the Creative Commons Attribution (CC BY) license (https://creativecommons.org/licenses/by/4.0/).

1. Introduction

Metamaterials are artificial composite structures or materials with extraordinary performance that have broad application prospects. Some metamaterials can effectively prevent wave propagation at specific frequencies, and the ranges of these frequencies are called bandgaps. The structures with bandgaps have aroused the research interest of people from diverse fields [1,2]. Metamaterials are widely used in noise reduction and isolation [3,4]. For example, the varying geometry or material configuration of the metamaterials to control certain frequencies and reduce vibration [5]. Also, these unique characteristics makes metamaterials ideal candidates for the design of pass-band directional mechanical filters [6] for directional wave transmission [7,8]. Shi, H.Y.Y. et al. [9] illustrates the possibility of tuning bandgaps with geometric variation. The influence of material properties on the bandgap characteristics of metamaterials has also been widely mentioned [10,11]. The problem is that the direction of wave propagation and bandgap cannot be tuned after manufacturing. Traditional methods of metamaterial design cannot achieve the continuous control of parameters. Thus, tunable metamaterials have received increasing amounts of attention from scholars.

Some studies have considered the influence of magnetic or electric fields on bandgap structures [12,13]. Piezoelectric materials are also taken into account [14,15]. Zi-Gui

et al. [16] found that temperature effects could potentially be used for fine-tuning of the phononic bandgap frequency. Jim, K.L. et al. [17] demonstrated the thermal tuning of phononic bandgaps in the megahertz range. These related studies have important guiding significances for better assisting in the design of tunable devices and tuning mechanisms.

The results of some studies indicate that the position and width of the bandgap are affected by the applied deformation [18,19]. Gao, N. et al. [20] confirms the feasibility of the design of soft tunable phononic crystals and acoustic devices by harnessing uniaxial tension. Structures with bandgaps are to be attenuated in a specific frequency range [21–24]. Geometry, material properties, and loading conditions all affect the tuning of the bandgap position of phonon crystals in the relevant research of Bertoldi, K. [19,25,26]. The soft materials can undergo finite and reversible elastic deformations because of super elasticity. And the porous structures are suitable for shape control. They can be used to make porous phonon crystals [11,27,28]. Their configuration can be easily tuned after manufacturing is completed through various methods. Generally, mechanical loading is simple and practical to exert on a structure. Bandgap characteristics will be changed in different geometric configurations with deformed porous materials [20,26,29].

Some metamaterial structures can also be deformed under different applied loads such as compression and stretching, which significantly affect their bandgap characteristics [11,30–32]. The applied load can close, open, and move the bandgap of the metamaterial structure, which can affect the wave propagation in a specific frequency range [29,33,34]. Li, N. et al. [11] proposed a new configuration-controllable porous metamaterial (CCPM) designed and manufactured using silicone rubber. The bandgap characteristics of CCPM were experimentally and numerically studied. Also, the vibration transmission characteristics of specimens with different deformations were tested, and the influence of the corresponding configuration change in the bandgap characteristics of the structure was studied. Through experimental and numerical analyses, it has been shown that the adjustment of the bandgap of CCPM could be achieved by controlling its configuration. In fact, the initial stress occurs during the configuration-control, and it also affects the bandgap characteristics when the configuration changes [35–38]. It can manipulate the band structure effectively [36] and can be used as a bandgap switch for the metamaterial structure [37,38]. Xinnan, L. et al. [39] found that the initial compressive stress will cause the bandgap to move towards low frequencies, while the initial tensile stress will cause the bandgap to move towards high frequencies.

The influence of configuration changes in the bandgap of CCPM in article [11] has been discussed in detail. However, the numerical calculation results of the bandgap are not very consistent with the experimental results, and there is a significant difference between them. In fact, initial stress occurs while the configuration changes, and the initial stress can have a certain influence on the bandgap of the structure [36–39]. And the initial stress has a more significant impact on CCPM. In this paper, initial stress refers to the average axial stress when axial loading displacement is applied to the structure in our manuscript. We use the same specimen of paper [11] to analyze the initial stress distribution and investigate the influence of the initial stress on the bandgap structure of the CCPM. The experimental platform was built to study the distribution of the initial stress of the CCPM under axial displacement, and the infinite element model of the CCPM was founded. Numerical results have a good agreement with the experimental data. In addition, the influence of the bandgap characteristics on the CCPM was studied, and the results were compared with that of paper [11]. Through the comparison, it is found that the bandgap structure considering the influence of the initial stress is more consistent with the experiment results of the transmittance spectra. Moreover, the specific effect of initial stress on the CCPM bandgap will be explored and discussed in detail.

2. Configuration-Controllable Porous Metamaterial Model and Stress Analysis

2.1. Configuration of Controllable Porous Metamaterials

The proposed porous metamaterial with a controllable configuration [11] is shown in Figure 1. The CCPM was designed with periodically arranged unit cells, and the shape of the unit cell could be adjusted through compression control. The structure can produce controlled deformation under simple external excitation, resulting in different band structures.

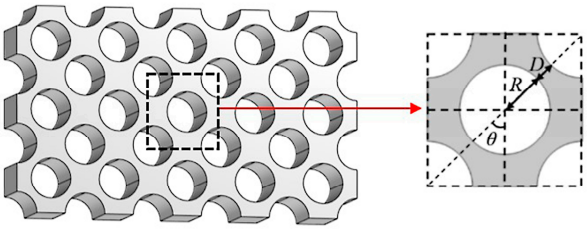

Figure 1. The schematic of the CCPM.

But under the external force, the periodic cell of the structure is deformed, the configuration changes accordingly, and the initial stress occurs at the same time. The presence of initial stress will also influence the bandgap distribution of the structure. In this paper, the distribution of the initial stress of the structure under different external forces is studied, and the influence of the initial stress on the bandgap of the structure is analyzed.

2.2. Stress Distribution Analysis

The stress distribution of the CCPM under different configuration changes was studied using experimental and finite element methods. The CCPM specimen is designed and manufactured from soft silicone rubber SR-2125 (the same specimen as article [11]); the specific structure is shown in Figure 2. Its length is 301.4 mm, width is 180.8 mm, and thickness is 50.0 mm. The silicon rubber properties are assumed to be linearly elastic and isotropic before buckling occurs in the CCPM. The geometric parameters and material properties of the CCPM are shown in Table 1.

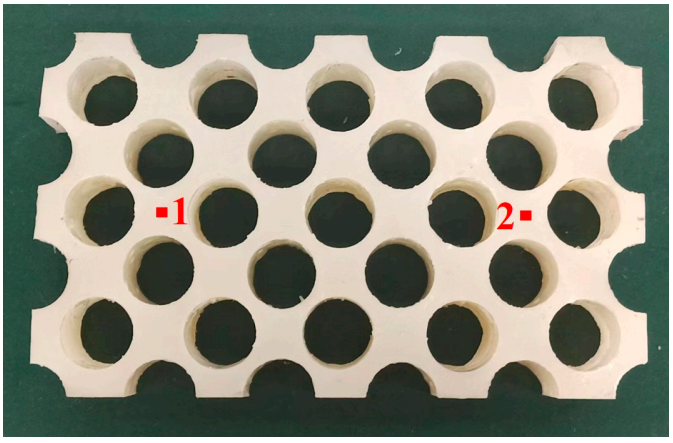

Figure 2. The specimen of the CCPM.

Table 1. Material properties and geometric parameters of the CCPM.

Material Parameters		Geometric Parameters	
Elastic modulus/(MPa)	0.870	R/(mm)	17.5
Poisson's ratio	0.499	D/(mm)	7.462
Density/(kg/m^3)	1230	θ/(deg)	45

In order to study the distribution of the initial stress of the structure with different controlled configurations, a strain test experimental platform was established, as shown in Figure 3. The experiment was conducted at room temperature. According to the size of CCPM, the XTDIC measuring head at the testing site was installed and the suitable measurement range was adjusted. Compressive loading of the specimen was performed by a microcomputer-controlled electro-hydraulic servo pressure testing machine (YAW-600) with a loading rate of 0.5 mm/min up to a maximum loading displacement of 30 mm. The top of the experimental piece is fixed, and the lower part is slowly compressed. During the loading process of CCPM, the XTDIC measurement system synchronously collects images using two cameras (the resolution is 5 million pixels, and the frame rate is 75 fps). Then, it automatically calculates the three-dimensional coordinates of the specimen during all loading stages to obtain the geometric displacement results via digital image correlation.

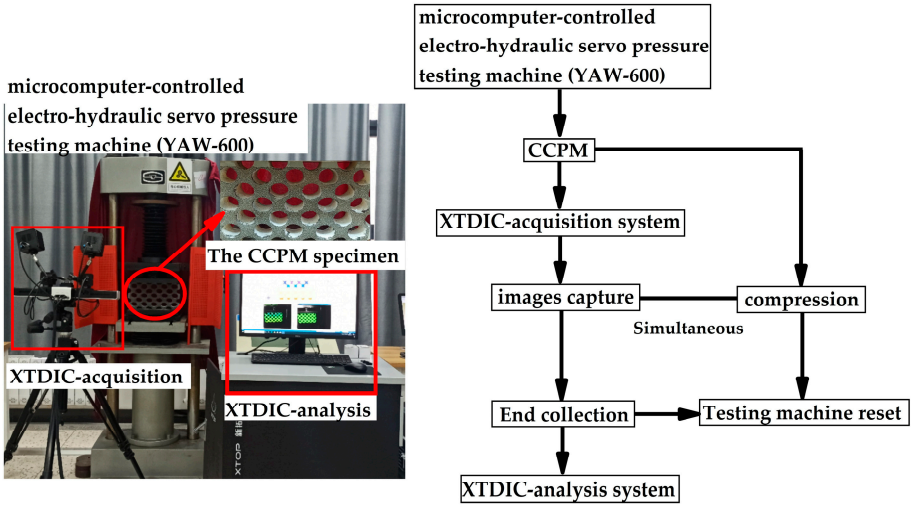

Figure 3. Experimental setup and procedure.

In addition, the finite element model of the structure is established with COMSOL, as shown in Figure 4. During the analysis process, the loading displacement is always limited (not exceeding 30 mm), and the deformation is relatively small. In this case, the structure will not buckle. Assuming that CCPM is thick enough, the analysis based on a plane strain model is sufficient [11]. Equivalent boundary conditions (marked in green) to the experiments are applied to the model. The top of the model is fixed, while the bottom is slowly compressed upwards with a loading displacement. The meshes of the computational domain are constructed using free trihedral meshing.

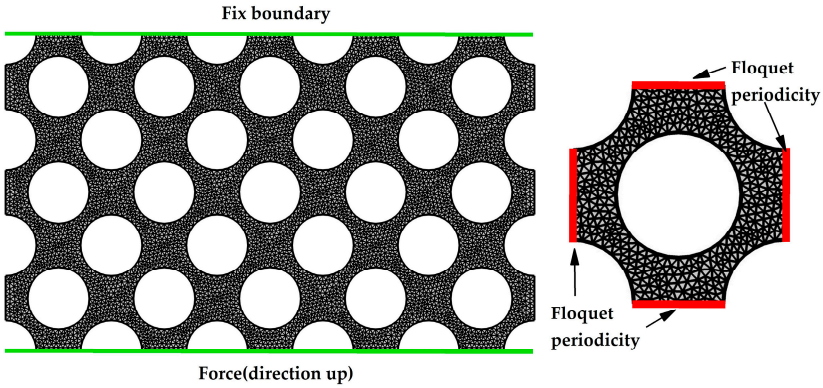

Figure 4. The FEM model of the CCPM. The unit cells and Floquet boundaries are also illustrated in this figure.

The deformation and displacement of the CCPM specimen are obtained and compared with the experimental results. Figure 5 presents the deformation, displacement, and stress distribution of the structure when the axial compression displacements of the CCPM are 0 mm, 10 mm, 20 mm, and 30 mm, respectively (changing sequentially from left to right). We can see that the configuration of the CCPM changes gradually as the axial displacement increases, and the shape of the holes changes from round to oval. Under the same force, the experimental results of the axial deformation shown in Figure 5b agree with the finite element results shown in Figure 5c well. Both results are consistent in terms of axial displacement. We observed that with an increase in axial displacement, the stress of the CCPM increases gradually in Figure 5d. The total stress gradually concentrated at the junction of each unit cell. And the maximum stress is concentrated near the round hole under the stress concentration. Due to the quasi-static nature of the load and relatively small compression, the linear finite element model can accurately simulate the deformation of the specimen. When the loading displacement is 10 mm, 20 mm, and 30 mm, the average axial stress of CCPM is 12,277 Pa, 20,325 Pa, and 25,648 Pa, respectively.

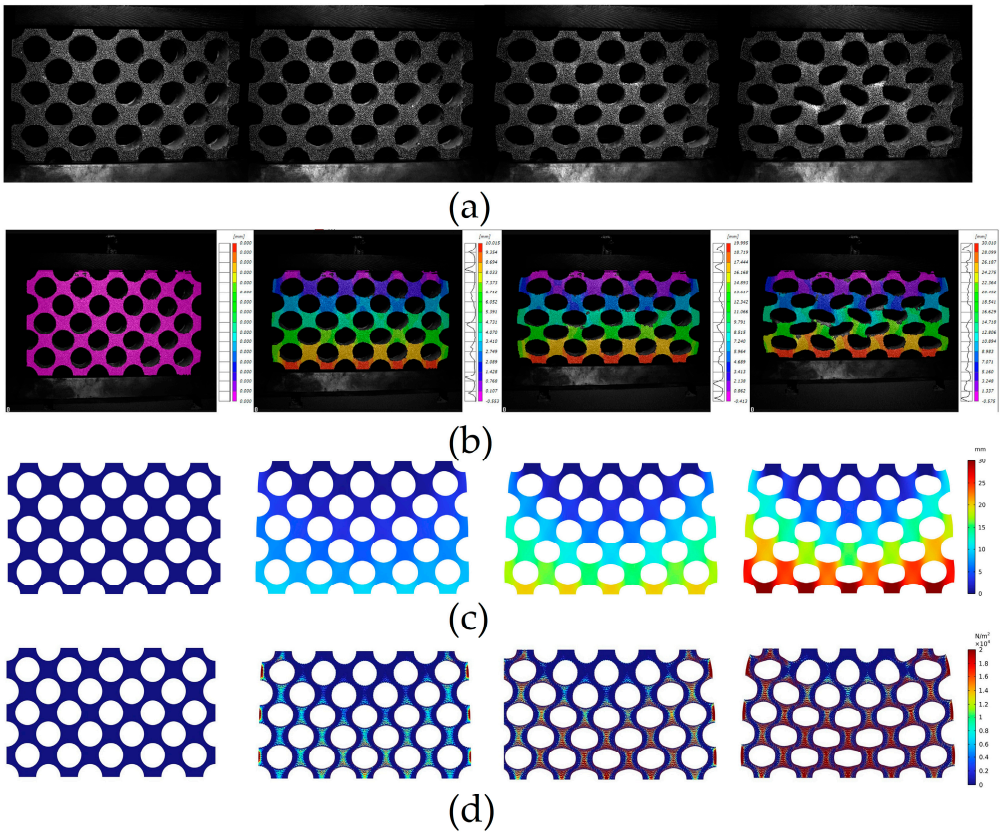

Figure 5. Comparison of experimental and finite element results of CCPM with uniaxial compression: (**a**) the CCPM with different configurations; (**b**) experimental displacements of CCPM; (**c**) finite element displacements of CCPM; (**d**) finite element stress distribution of CCPM.

Points 1 and 2, shown in Figure 2, are taken as the two observation points. Table 2 lists the stress of the experiment and finite element results for the two points. Based on the numerical and experimental results, the relationship between the stress and displacement of the observation points was established. Figure 6 depicts the axial stress with different axial displacement of the two points. It is clear that the stress increases linearly with the increase in axial displacement, and the numerical results are in good agreement with that of the experiment.

Table 2. Experimental values and finite element results of stress at observation points.

		5 mm	10 mm	15 mm	20 mm	25 mm	30 mm
Point 1	FEM (Pa)	8961	17,574	25,752	33,582	40,803	47,589
	EXP (Pa)	8526	18,531	24,621	35,844	44,370	52,287
	error	4.85%	5.45%	4.39%	6.74%	8.74%	9.87%
Point 2	FEM (Pa)	9222	18,009	26,274	34,191	41,412	48,198
	EXP (Pa)	8874	17,052	27,579	32,016	38,367	43,848
	error	3.77%	5.31%	4.97%	6.36%	7.35%	9.03%

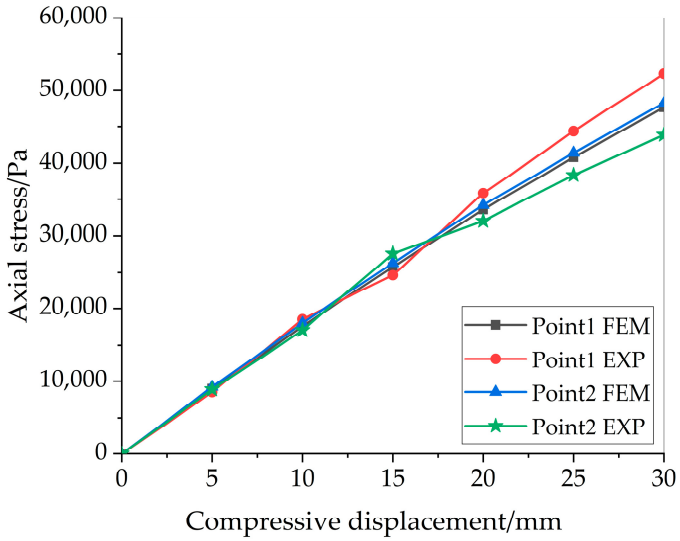

Figure 6. The relationship between compression displacement and axial stress.

3. Numerical Result of Bandgap Characteristics

3.1. Effect of Initial Stress on the Bandgap Characteristics

The finite element method has been employed to the bandgap calculation of CCPM.

When the configuration changes, the lattice constant of CCPM changes, resulting in complex boundary conditions. Although, under complex boundary conditions, the eigenvalue of CCPM can be solved directly using COMSOL.

The periodicity of CCPM enables calculations to be implemented in a unit cell. The stress of the CCPM under different axial displacement is obtained first. Then, the initial stress is adopted as a precondition into the numerical bandgap calculations. Floquet periodicity boundaries are applied to the unit cell. The meshes of the computational domain are constructed using free trihedral meshing, and the Floquet boundaries are marked in red (Figure 4). The effect of the initial stress on the bandgap characteristics of the CCPM is discussed and compared with the experimental results cited in paper [11].

Figure 7 depicts the comparison between the bandgap diagram and transmittance spectra when the axial compression deformation is 10 mm. Figure 7a,b are the bandgap diagrams in the range of 0 Hz to 450 Hz with and without considering initial stress. Figure 7c is the experimental transmission spectra cited from paper [11]. It can be seen that two bandgaps appear between 0 Hz and 450 Hz. Without considering the initial stress, the frequency range of the first bandgap is 262 Hz–310 Hz and that of the second bandgap is 394 Hz–405 Hz. Considering the initial stress, the frequency range of the first and second bandgaps is converted into 254 Hz–291 Hz and 391 Hz–400 Hz. Their beginning and ending frequencies decrease, and the width of the two bandgaps is reduced when the initial stress is considered. Compared with Figure 7a, considering the initial stress, the two bandgap frequency ranges are more in accordance with the experimental transmission spectra. From the comparison in Figure 7, we may reach the conclusion that

initial stress occurs as the configuration of CCPM changes and has a significant influence on its bandgap characteristics.

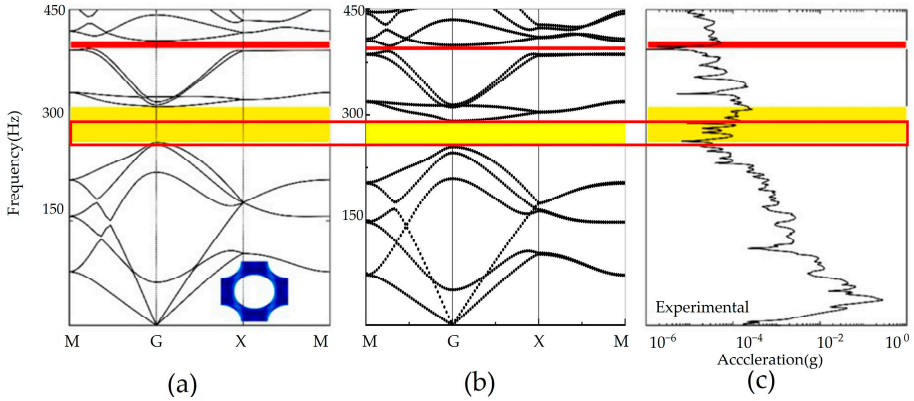

Figure 7. Comparison between the bandgap diagram and transmittance spectra: (**a**) without initial stress, (**b**) with initial stress, (**c**) transmission spectra (cites from paper [11]).

3.2. Effect of the Initial Compressive Stress on the Bandgap Characteristics

The comparison of bandgap results in Table 3 shows that the finite element results in this paper are consistent with those in reference [11]. In order to study the influence of initial stress on the bandgap of CCPM, we calculated the bandgap characteristics by considering the initial stress of the structure under different compression deformations. Figure 8 plots the bandgap distributions of different compression displacement. The bandgaps with axial compressive displacements of 0 mm, 5 mm, 10 mm, 15 mm, 20 mm, 25 mm, and 30 mm are given. Figure 8a,b are two bandgap diagrams with and without considering the initial compressive stress. From Figure 8b, we can see that the first bandgap (colored in yellow) begins to contract and move upwards, and the second additional bandgap (colored in red) begins to open and gradually widens as the compression displacement increases. Compared with Figure 8b, as the compression displacement increases, the initial stress begins to change. When considering initial stress [see Figure 8a], the first bandgap (colored in yellow) also begins to contract but moves downwards. The second additional bandgap (colored in red) begins to open. In addition, the third brand new additional bandgap (colored in blue) emerges. Numerical results show that after the compression displacement of 20 mm (the average initial axial stress of the CCPM reaches 20,325 Pa), the third additional bandgap (colored in blue) appears and begins to widen. After the compression displacement of 25 mm (the average initial axial stress of the CCPM reaches 23,273 Pa), the first initial bandgap closes. The comparison of Figure 8a,b demonstrates how the initial stress can be used to effectively modify the bandgaps in the structure.

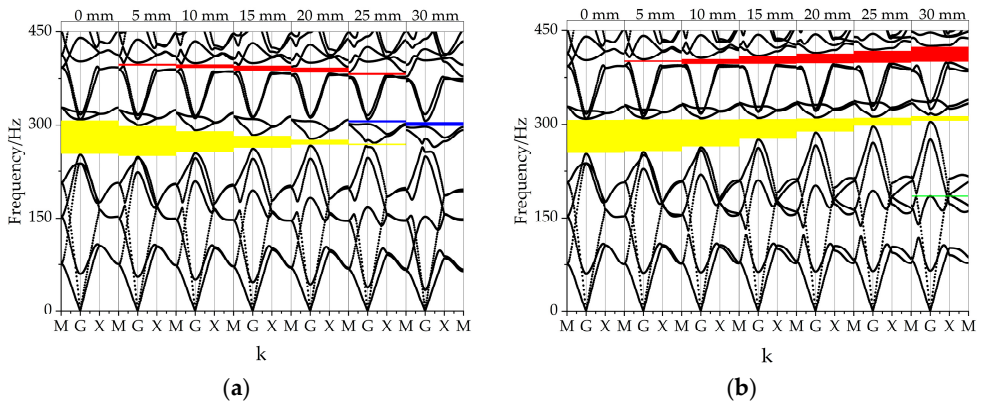

Figure 8. The bandgap of the CCPM at different compressive displacements: (**a**) with initial stress; (**b**) without initial stress.

Table 3. A comparison with equivalent research [11].

Loading Displacement	10 mm	20 mm	30 mm
Bandgap results obtained from reference [11]	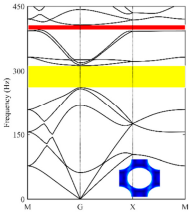	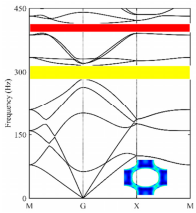	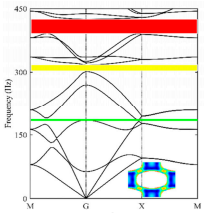
Bandgap results obtained from the FEM in this study	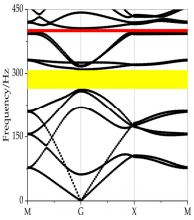	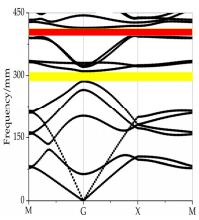	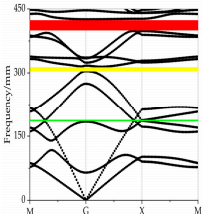

Figure 9 shows the specific bandgap distribution of CCPM under different compression displacements. It can be seen from Figure 9a that the width of the first initial bandgap gradually decreases as the amount of compression increases. Its beginning and ending frequencies are shifted towards low frequencies considering initial stress. The first initial bandgap closes after the compression displacement reaches 30 mm (the average initial axial stress of the structure reaches 25,648 Pa). As shown in Figure 9b, the second additional bandgap appears as the amount of compression increases. The bandgap width is proportional to the compression displacement without initial stress. In the case of considering initial stress, its bandgap width shows a nonlinear trend in Figure 9b. Specifically, the width of the bandgap increases from 0 Hz to a maximum of 13 Hz and then decreases again. Moreover, the beginning and ending frequencies of the second additional bandgap shift down.

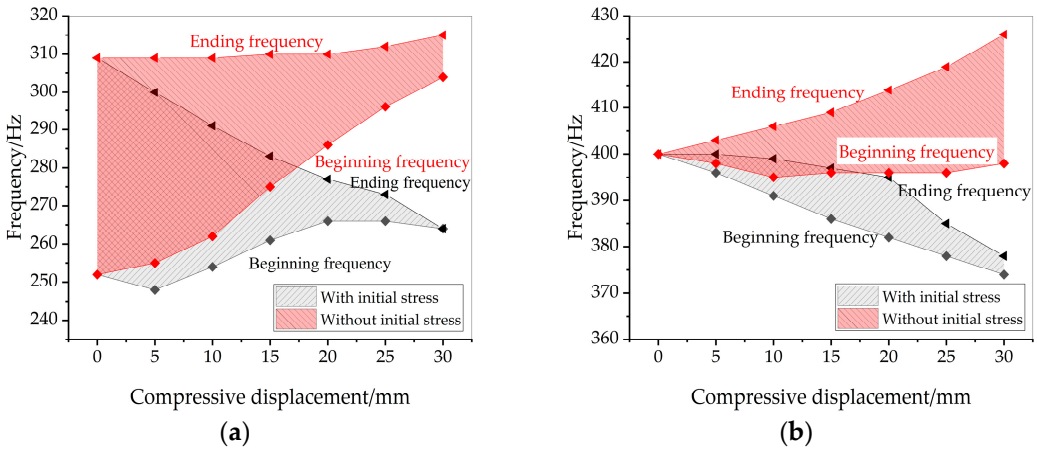

Figure 9. Specific bandgap variations: (**a**) first initial bandgap; (**b**) second additional bandgap.

3.3. Effect of the Initial Tensile Stress on the Bandgap Characteristics

Initial tensile stress occurs when the CCPM is stretched. Figure 10a,b show the changes in the bandgap diagrams with and without considering initial stress corresponding to the tensile displacement of the CCPM of 0 mm, 5 mm, 10 mm, 15 mm, 20 mm, 25 mm, and 30 mm from left to right. By comparing Figure 10a,b, it is indicated that initial tensile stress has obvious great effects on the bandgap characteristics.

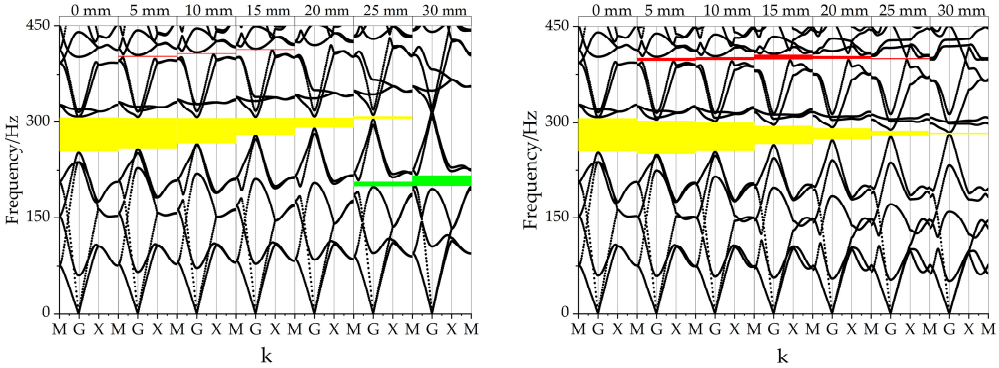

Figure 10. The bandgap of the CCPM at different tensile displacements: (**a**) with initial stress; (**b**) without initial stress.

As shown in Figure 10b, the tensile loading displacement increases from 0 mm to 30 mm. The first initial bandgap (colored in yellow) begins to contract and move towards a low frequency. And the second additional bandgap (colored in red) appears and disappears again. However, in Figure 10a, as the initial tensile stress increases, the first initial bandgap (colored in yellow) begins to contract and move upwards. And the second additional bandgap (colored in red) and the third bandgap (colored in green) are opened gradually. The third additional bandgap has not appeared in Figure 10b. Based on Figure 10, the third additional bandgap (colored in green) appears and begins to widen when the tensile displacement exceeds 20 mm (the average axial average initial stress reaches 49,406 Pa). Compared to Figure 10b, the initial stress can close the second additional bandgap in advance, as shown in Figure 10a. Moreover, the first initial bandgap is closed at the tensile displacement of 30 mm (the average axial initial stress reaches 96,261 Pa).

The detailed bandgap distribution of CCPM under different tensile displacements is illustrated in Figure 11. The width of the first initial bandgap gradually decreases as the tensile displacement increases [see Figure 11a]. Considering initial stress, the beginning and ending frequencies of the first initial bandgap both move towards high frequencies, as shown in Figure 11a. And the bandgap closes when the tensile displacement is 30 mm (the average axial initial stress reaches 96,261 Pa). Next, Figure 11b investigates the changes in the second additional bandgap. It begins to appear with an increase in tensile displacement. The width of the bandgap increases from 0 Hz to a maximum of 11 Hz and decreases again without initial stress. However, when the initial stress is taken into account, its bandgap width is significantly reduced at the stages of individual deformations. Both the beginning and ending frequencies shift up. As is seen, the second additional bandgap will be closed when the tensile displacement is 20 mm (average axial initial stress is 49,406 Pa).

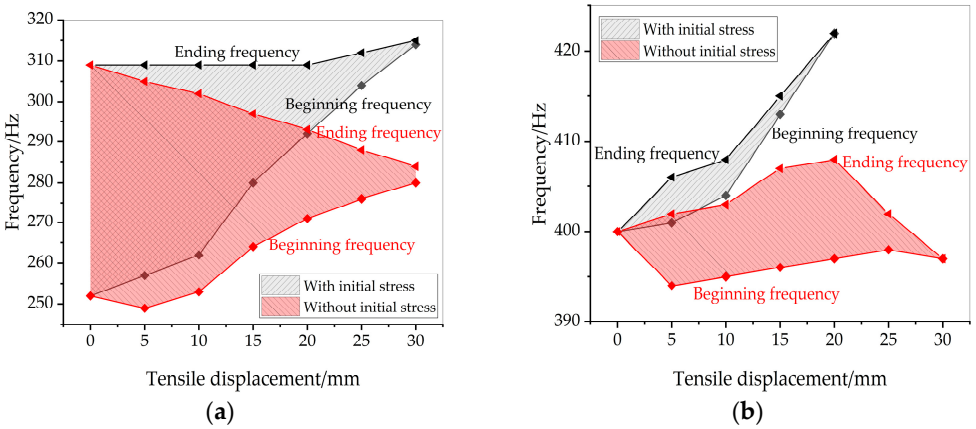

Figure 11. Specific bandgap variations: (**a**) first initial bandgap; (**b**) second additional bandgap.

The variation in the center frequency of the first initial bandgap with displacement is plotted [see Figure 12] to demonstrate the dependence of initial stress on the position of bandgaps. As can be seen from Figure 12, considering the initial stress during compression causes the center frequency of the bandgap of the structure to drop, while considering the initial stress during stretching is the opposite. This is consistent with the results reported by Xinnan, L. [39]. The changing trend of center frequency about tensile is the opposite. With a continuous increase in tensile displacement, the center frequency of the bandgap with initial stress increases more. Figure 13 presents the width of the first initial bandgap which varies in different configurations. It is clear that the initial stress reduces the bandgap width. Thus, an external extension or compression can be used to effectively modify the bandgaps in the structure, which can undergo large geometric deformations under tension or compression [32]. According to the elastic dynamic theory, when waves propagate in a two-dimensional uniform elastic medium (neglecting body force), Equation (1) can be established [11].

$$-\rho(\boldsymbol{r})\omega^2\boldsymbol{u}(\boldsymbol{r},t) = (\lambda(\boldsymbol{r}) + \mu(\boldsymbol{r}))\nabla\nabla\cdot\boldsymbol{u}(\boldsymbol{r},t) + \mu\nabla^2\boldsymbol{u}(\boldsymbol{r},t) \tag{1}$$

$\boldsymbol{u} = \{u_x, u_y\}^T$ is the displacement column vector, $\nabla\cdot\boldsymbol{u} = \frac{\partial u_x}{\partial x} + \frac{\partial u_y}{\partial y}$ is divergence, $\boldsymbol{r}$ is the position coordinates of CCPM, $\rho(\boldsymbol{r})$ is the material density, and $\lambda(\boldsymbol{r})$ and $\mu(\boldsymbol{r})$ are the Lamé coefficients. In a unit cell of CCPM, Equation (1) can be discretized as follows:

$$(\boldsymbol{K} - \omega^2\boldsymbol{M})\boldsymbol{U} = 0 \tag{2}$$

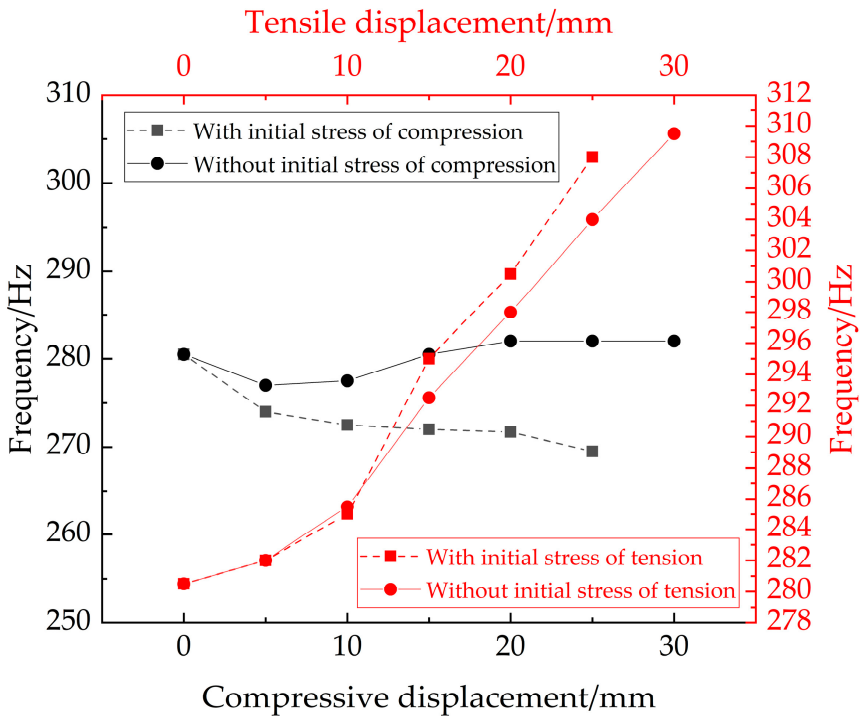

Figure 12. Variation in the center frequency of the first initial bandgap.

$\boldsymbol{K}$ is the stiffness matrices; $\boldsymbol{M}$ is the mass matrices. It shows that the ω is related to the $\boldsymbol{K}$ of CCPM. The stiffness of CCPM is not only affected by array configuration but also by initial stress. Thus, the influence of the initial stress generated by the structure on the bandgap at the same time as the configuration change cannot be ignored.

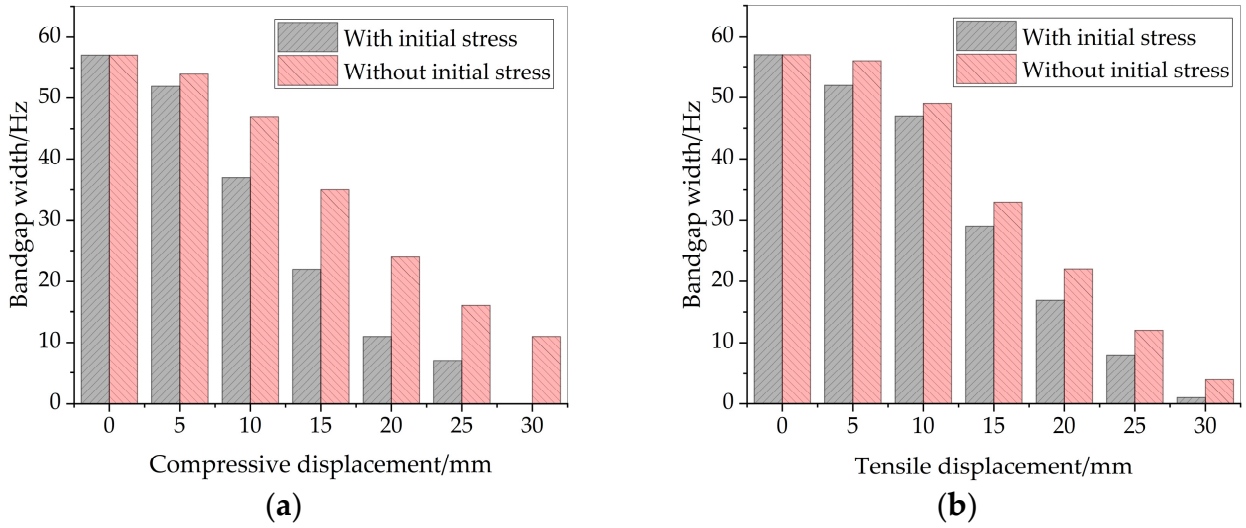

Figure 13. The first initial bandgap width changes with the deformation mode: (**a**) compression; (**b**) tension.

4. Conclusions

In this paper, the distribution of the initial stress of the configuration-controllable metamaterial under axial displacement was analyzed using numerical and experimental methods. And the influence of initial stress on the bandgap characteristics of the structure was compared with the results without considering initial stress. The numerical results showed that the bandgap characteristics of the CCPM with initial stress are more in accordance with the published experimental transmission spectra. This indicated that initial stresses have a significant influence on bandgap characteristics as the configuration of CCPM changes. The research further revealed the reasons for the errors between numerical and experimental data for paper [11].

As the initial tensile or compressive stress increases, the first initial bandgap contracts and new bandgaps occur. Existing bandgaps will be closed or new ones will be opened when the initial stress turns to a certain value. This feature can be considered when controlling vibrations of multiple frequencies. Considering the initial compressive stress, the first initial bandgap is reduced to 254 Hz–291 Hz and the second additional bandgap is reduced to 391 Hz–400 Hz when the CCPM is compressed by the displacement of 10 mm. The third additional bandgap occurs as the compression and tension displacements reach 20 mm. The tensile initial stress shifts up the bandgaps, while the compressive initial stress shifts them down. This feature can be used for vibration reduction at high and low frequencies.

Author Contributions: Conceptualization, H.Z. and J.W.; methodology, F.Y., H.Z. and J.W.; software, F.Y. and Q.F.; validation, Q.F.; data curation, F.Y.; writing—original draft preparation, F.Y.; writing—review and editing, H.Z. and J.W.; supervision, H.Z. All authors have read and agreed to the published version of the manuscript.

Funding: This research received no external funding.

Institutional Review Board Statement: Not applicable.

Informed Consent Statement: Not applicable.

Data Availability Statement: All data generated and analyzed during this study are included in this article.

Conflicts of Interest: The authors declare no conflict of interest.

References

1. Maldovan, M. Sound and heat revolutions in phononics. *Nature* **2013**, *503*, 209–217. [CrossRef] [PubMed]
2. Cummer, S.A.; Christensen, J.; Alu, A. Controlling sound with acoustic metamaterials. *Nat. Rev. Mater.* **2016**, *1*, 16001. [CrossRef]
3. Casadei, F.; Dozio, L.; Ruzzene, M.; Cunefare, K.A. Periodic shunted arrays for the control of noise radiation in an enclosure. *J. Sound Vib.* **2010**, *329*, 3632–3646. [CrossRef]
4. Ruzzene, M.; Scarpa, F.; Soranna, F. Wave beaming effects in two-dimensional cellular structures. *Smart Mater. Struct.* **2003**, *12*, 363–372. [CrossRef]
5. Cinefra, M.; D'Amico, G.; Miguel, A.G.D.; Filippi, M.; Carrera, E. Efficient numerical evaluation of transmission loss in homogenized acoustic metamaterials for aeronautical application. *Appl. Acoust.* **2020**, *164*, 107253. [CrossRef]
6. Ruzzene, M.; Scarpa, F. Directional and band-gap behavior of periodic auxetic lattices. *Phys. Status Solidi* **2005**, *242*, 665–680. [CrossRef]
7. Zhao, D.; Wang, Y.T.; Fung, K.H.; Zhang, Z.Q.; Chan, C.T. Acoustic metamaterials with spinning components. *Phys. Rev. B* **2020**, *101*, 054107. [CrossRef]
8. Han, X.K.; Zhang, Z. Acoustic beam controlling in water by the design of phononic crystal. *Extrem. Mech. Lett.* **2019**, *34*, 100602. [CrossRef]
9. Shi, H.Y.Y.; Tay, T.E.; Lee, H.P. Elastic wave propagation in perforated plates with tetrad elliptical structural hierarchy: Numerical analysis and experimental verification. *J. Sound. Vib.* **2019**, *448*, 73–82.
10. Zhou, X.Z.; Wang, Y.S.; Zhang, C. Effects of material parameters on elastic band gaps of two-dimensional solid phononic crystals. *J. Appl. Phys.* **2009**, *106*, 2022. [CrossRef]
11. Li, N.; Bai, C.Q.; Liu, M.B. Configuration-controllable porous metamaterial and its bandgap characteristics: Experimental and numerical analysis. *J. Sound Vib.* **2022**, *535*, 117107. [CrossRef]
12. Matar, O.B.; Robillard, J.F.; Vasseur, J.O.; Hladky-Hennion, A.C.; Deymier, P.A.; Pernod, P.; Preobrazhensky, V. Band gap tunability of magneto-elastic phononic crystal. *J. Appl. Phys.* **2012**, *111*, 054901. [CrossRef]
13. Yeh, J.-Y. Control analysis of the tunable phononic crystal with electrorheological material. *Phys. B Condens. Matter* **2007**, *400*, 137–144. [CrossRef]
14. Zou, X.-Y.; Chen, Q.; Liang, B.; Cheng, J.-C. Control of the elastic wave bandgaps in two-dimensional piezoelectric periodic structures. *Smart Mater. Struct.* **2008**, *17*, 015008. [CrossRef]
15. Casadei, F.; Delpero, T.; Bergamini, A.; Ermanni, P.; Ruzzene, M. Piezoelectric resonator arrays for tunable acoustic waveguides and metamaterials. *J. Appl. Phys.* **2012**, *112*, 064902. [CrossRef]
16. Huang, Z.-G.; Wu, T.-T. Temperature effect on the bandgaps of surface and bulk acoustic waves in two-dimensional phononic crystals. *IEEE Trans. Ultrason. Ferroelectr. Freq. Control.* **2005**, *52*, 365–370. [CrossRef] [PubMed]
17. Jim, K.L.; Leung, C.W.; Lau, S.T.; Choy, S.H.; Chan, H.L.W. Thermal tuning of phononic bandstructure in ferroelectric ceramic/epoxy phononic crystal. *Appl. Phys. Lett.* **2009**, *94*, 193501. [CrossRef]
18. Wang, L.; Bertoldi, K. Mechanically tunable phononic band gaps in three-dimensional periodic elastomeric structures. *Int. J. Solids Struct.* **2012**, *49*, 2881–2885. [CrossRef]
19. Bertoldi, K.; Boyce, M.C. Wave propagation and instabilities in monolithic and periodically structured elastomeric materials undergoing large deformations. *Phys. Rev. B* **2008**, *78*, 184107. [CrossRef]
20. Gao, N.; Li, J.; Bao, R.H.; Chen, W.Q. Harnessing uniaxial tension to tune Poisson's ratio and wave propagation in soft porous phononic crystals: An experimental study. *Soft Matter* **2019**, *15*, 2921–2927. [CrossRef]
21. Kumar, N.; Pal, S. Low frequency and wide band gap metamaterial with divergent shaped star units: Numerical and experimental investigations. *Appl. Phys. Lett.* **2019**, *115*, 254101. [CrossRef]
22. Lu, K.; Zhou, G.J.; Gao, N.S.; Li, L.Z.; Lei, H.X.; Yu, M.R. Flexural vibration bandgaps of the multiple local resonance elastic metamaterial plates with irregular resonators. *Appl. Acoust.* **2020**, *159*, 107115. [CrossRef]
23. Zhang, Q.; Zhang, K.; Hu, G.K. Tunable fluid-solid metamaterials for manipulation of elastic wave propagation in broad frequency range. *Appl. Phys. Lett.* **2018**, *112*, 221906. [CrossRef]
24. Zeng, Y.; Xu, Y.; Yang, H.W.; Muzamil, M.; Xu, R.; Deng, K.K.; Peng, P.; Du, Q.J. A Matryoshka-like seismic metamaterial with wide band-gap characteristics. *Int. J. Solids Struct.* **2020**, *185*, 334–341. [CrossRef]
25. Casadei, F.; Bertoldi, K. Harnessing fluid-structure interactions to design self-regulating acoustic metamaterials. *J. Appl. Phys.* **2014**, *115*, 034907. [CrossRef]
26. Wang, P.; Shim, J.; Bertoldi, K. Effects of geometric and material nonlinearities on tunable band gaps and low-frequency directionality of phononic crystals. *Phys. Rev. B* **2013**, *88*, 014304. [CrossRef]
27. Singamaneni, S.; Bertoldi, K.; Chang, S.; Jang, J.H.; Thomas, E.L.; Boyce, M.C.; Tsukruk, V.V. Instabilities and Pattern Transformation in Periodic, Porous Elastoplastic Solid Coatings. *ACS Appl. Mater. Interfaces* **2009**, *1*, 42–47. [CrossRef]
28. Babaee, S.; Wang, P.; Bertoldi, K. Three-dimensional adaptive soft phononic crystals. *J. Appl. Phys.* **2015**, *117*, 244903. [CrossRef]
29. Shan, S.C.; Kang, S.H.; Wang, P.; Qu, C.Y.; Shian, S.; Chen, E.R.; Bertoldi, K. Harnessing Multiple Folding Mechanisms in Soft Periodic Structures for Tunable Control of Elastic Waves. *Adv. Funct. Mater.* **2014**, *24*, 4935–4942. [CrossRef]
30. Huang, Y.; Zhang, C.L.; Chen, W.Q. Tuning Band Structures of Two-Dimensional Phononic Crystals With Biasing Fields. *J. Appl. Mech-T Asme* **2014**, *81*, 091008. [CrossRef]

31. Huang, Y.; Shen, X.D.; Zhang, C.L.; Chen, W.Q. Mechanically tunable band gaps in compressible soft phononic laminated composites with finite deformation. *Phys. Lett. A* **2014**, *378*, 2285–2289. [CrossRef]
32. Huang, Y.L.; Gao, N.; Chen, W.Q.; Bao, R.H. Extension/Compression-Controlled Complete Band Gaps in 2D Chiral Square-Lattice-Like Structures. *Acta Mech. Solida Sin.* **2018**, *31*, 51–65. [CrossRef]
33. Wang, P.; Casadei, F.; Shan, S.C.; Weaver, J.C.; Bertoldi, K. Harnessing Buckling to Design Tunable Locally Resonant Acoustic Metamaterials. *Phys. Rev. Lett.* **2014**, *113*, 014301. [CrossRef] [PubMed]
34. Gao, N.; Huang, Y.L.; Bao, R.H.; Chen, W.Q. Robustly Tuning Bandgaps in Two-Dimensional Soft Phononic Crystals with Criss-Crossed Elliptical Holes. *Acta Mech. Solida Sin.* **2018**, *31*, 672. [CrossRef]
35. Rogerson, G.A.; Sandiford, K.J. The effect of finite primary deformations on harmonic waves in layered elastic media. *Int. J. Solids Struct.* **2000**, *37*, 2059–2087. [CrossRef]
36. Parnell, W.J. Effective wave propagation in a pre-stressed nonlinear elastic composite bar. *IMA J. Appl. Math.* **2007**, *72*, 223–244. [CrossRef]
37. Barnwell, E.G.; Parnell, W.J.; Abrahams, I.D. Antiplane elastic wave propagation in pre-stressed periodic structures; tuning, band gap switching and invariance. *Wave Motion* **2016**, *63*, 98–110. [CrossRef]
38. Zhou, X.L.; Chen, C.Q. Tuning the locally resonant phononic band structures of two-dimensional periodic electroactive composites. *Phys. B* **2013**, *431*, 23–31. [CrossRef]
39. Xinnan, L.; Yan, L.; Yingbo, J.I. Attenuation zones of initially stressed periodic local resonant Mindlin plates. *J. Vib. Shock* **2019**, *38*, 228–232+255. [CrossRef]

Disclaimer/Publisher's Note: The statements, opinions and data contained in all publications are solely those of the individual author(s) and contributor(s) and not of MDPI and/or the editor(s). MDPI and/or the editor(s) disclaim responsibility for any injury to people or property resulting from any ideas, methods, instructions or products referred to in the content.